J. Cent. South Univ. (2020) 27: 3625−3636
DOI: https://doi.org/10.1007/s11771-020-4570-0

Springer

Synthesis of a novel hexagonal porous TT-Nb_2O_5 via solid state reaction for high-performance lithium ion battery anodes

ZHOU Yu(周玉), LIU Ke(刘柯), ZHOU Yue(周悦), NI Jia-hua(倪佳华), DOU Ai-chun(窦爱春), SU Ming-ru(苏明如), LIU Yun-jian(刘云建)

School of Materials Science and Technology, Jiangsu University, Zhenjiang 212013, China

Abstract: Hexagonal porous Nb_2O_5 was synthesized for the first time via a facile solid-state reaction. The structure and electrochemical properties have been optimized through tuning heating temperature. X-ray diffraction results indicate that pseudo hexagonal Nb_2O_5 (TT-Nb_2O_5) and orthorhombic Nb_2O_5 have been synthesized at different temperatures. Hexagonal sheet and porous structure of Nb_2O_5 were characterized by scanning electron microscopy and N_2-adsorption-desorption isotherms. The as-prepared TT-Nb_2O_5 (heated at 600 °C) shows the best performance with a remarkable charge capacity of 178 mA·h/g at 0.2*C*, which is higher than that of T-Nb_2O_5. Even at 20*C*, TT-Nb_2O_5 offers unprecedented rate capability up to 86 mA·h/g. The high rate capacity is due to pseudocapacitive Li^+ intercalation mechanism of TT-Nb_2O_5. The reported results demonstrate that Nb_2O_5 with good crystal structure and high specific surface area is a powerful composite design for high-rate and safe anode materials.

Key words: lithium-ion battery; Nb_2O_5; hexagonal porous sheet; electrochemical performance

Cite this article as: ZHOU Yu, LIU Ke, ZHOU Yue, NI Jia-hua, DOU Ai-chun, SU Ming-ru, LIU Yun-jian. Synthesis of a novel hexagonal porous TT-Nb_2O_5 via solid state reaction for high-performance lithium ion battery anodes [J]. Journal of Central South University, 2020, 27(12): 3625−3636. DOI: https://doi.org/10.1007/s11771-020-4570-0.

1 Introduction

Lithium ion batteries (LIBs) have been widely applied for electric vehicles (EV) and portable electronic products due to their high energy density and long cycle life [1−6]. However, the low insertion voltage and poor rate performance of commercial graphite anode will cause formation of Li dendrite at high current density, which is difficult to meet the growing demands for EV with high security [7−9]. Among all the anode materials, $Li_4Ti_5O_{12}$ has been considered successful anode for its suitable working voltage and excellent cycle performance [10−12]. Operating voltage between 1.0 and 2.0 V can suppress the generation of SEI layer and lithium dendrites. But the maximum capacity of $Li_4Ti_5O_{12}$ is only 175 mA·h/g. Nb_2O_5 attracts particular attention because of its higher theoretical specific capacity (~200 mA·h/g) and excellent rate performance at suitable operating voltage [13, 14].

Nb_2O_5 has been synthesized with many crystal structures by controlling annealing temperature, such as pseudo hexagonal Nb_2O_5 (TT-Nb_2O_5), orthorhombic Nb_2O_5 (T-Nb_2O_5), tetragonal Nb_2O_5 (M-Nb_2O_5), and monoclinic Nb_2O_5 (H-Nb_2O_5) [15]. Nb_2O_5 with different crystal structures shows different lithium storage performances. In previous reports [16], T-Nb_2O_5 exhibits the best

Foundation item: Projects(51974137, 51774150) supported by the National Natural Science Foundation of China; Project(2020M671361) supported by China Postdoctoral Science Foundation
Received date: 2020-06-02; **Accepted date:** 2020-09-14
Corresponding author: LIU Yun-jian, PhD, Professor; Tel/Fax: +86-511-88790190; E-mail: lyjian122331@163.com; ORCID: https://orcid.org/0000-0002-8729-1351

development of nanomaterials, TT-Nb_2O_5 with high specific surface area can also show the high capacity and rate performance [17, 18]. It was found that the rapid pseudocapacitive charge storage mechanism plays an essential role in retaining the energy density and rate performance of TT-Nb_2O_5 [19]. Therefore, the electrochemical performance of Nb_2O_5 is not only determined by the crystal structures, but also influenced by the specific surface area. Nb_2O_5 with different nanostructure or porous structure has been prepared for LIBs [20−22]. However, there is no systematic research on the electrochemical performance of Nb_2O_5 with different crystal structures and specific surface area. Moreover, the traditional solvothermal or hydrothermal methods are too complex to precisely control the synthesis process [23, 24]. Hence, it is necessary to synthesize Nb_2O_5 with different crystal structures and specific surface area by a practical method.

In this paper, the micron-sized porous hexagonal sheets TT-Nb_2O_5 and T-Nb_2O_5 were first synthesized with hexagonal $NbSe_2$ as rare material by facile solid-state reaction. The specific surface area of TT-Nb_2O_5 sheets was higher than that of T-Nb_2O_5, which could deliver higher capacity and better cycling performance at large current density (86 mA·h/g at 20*C*). Furthermore, high ratio of the intercalation pesudocapacitance of TT-Nb_2O_5 has been demonstrated as a dominant contribution to the excellent rate capability.

2 Material and methods

2.1 Synthesis

The porous flake Nb_2O_5 was synthesized through a solid-state reaction and the synthesis schematic process is shown in Figure 1. The starting materials niobium and selenium powders were weighed according to the molar ratio (Se excess 4%). After ball-milling for 8 h, the mixture was conveyed to a crucible and calcined at 700 °C for 2 h in Ar atmosphere for the preparation of the hexagonal $NbSe_2$ sheet. Finally, the porous flake Nb_2O_5 was obtained by annealing of as-prepared solid product at 400, 500, 600 and 700 °C for 2 h in air, and the as-prepared Nb_2O_5 samples were marked as NbO_4, NbO_5, NbO_6 and NbO_7, respectively.

2.2 Characterization

The crystal structure of as-prepared Nb_2O_5 was characterized by X-ray powder diffraction (XRD) on the Ultima IV with Cu K_α radiation in the 2θ range of 10°−70°. The morphology and the element mapping of the samples were collected on FEI Nova Nano 450 SEM. Transmission electron microscopy (TEM) images were performed with FEI Tecnai F20 with acceleration voltage of 200 kV. X-ray photoelectron spectroscopy (XPS) data were also collected by PHI-5000 versaprobe for further analysis.

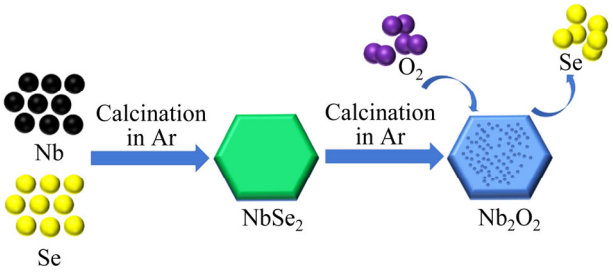

Figure 1 Synthesis schematic process of hexagonal porous sheet Nb_2O_5

2.3 Electrochemistry testing

The porous sheet Nb_2O_5 was ground with acetylene black and polyvinylidene fluoride in a mass ratio of 7:2:1 and then dispersed into 1-methyl-2-pyrrolidinone to mix evenly. The slurry was passed onto the copper foils. After being dried in vacuum at 80 °C for 24 h, the electrode was punched into disks with diameter of 12 mm. The mass loading of the active materials was about 1.2 mg/cm^2. CR2025 cells were assembled in the argon-filled glove box. 1 mol/L $LiPF_6$ in diethyl carbonate (DMC)/ethylene carbonate (EC) (1:1 volume ratio) was used as the electrolyte. Celgard 2500 polypropylene separator was selected as the separator and the pure lithium metal was the counterpart electrode. The galvanostatic discharge/charge of the half cells was examined by NEWWARE battery testing system at 25 °C in the voltage range of 1−3 V (vs Li^+/Li). The cyclic voltammetry (CV) tests and electrochemical impedance spectroscopy (EIS) results were collected on CHI660D electrochemical workstation.

3 Results and discussion

3.1 Structure and morphology characterization

Figure 2(a) shows the XRD patterns of the

Nb_2O_5 calcined at various temperatures ranging from 400 to 700 °C. The peaks of NbO_4, NbO_5 and NbO_6 accord well with the standard data of pseudohexagonal structure Nb_2O_5 (TT-Nb_2O_5, PDF#28-0317). The XRD peaks (001), (100) and (101) with the increase of calcination temperature become more and more stronger, which indicates that the higher crystalline nature of samples [25]. When the temperature reaches 700 °C, the diffraction peaks of NbO_7 sample could be indexed to the typical orthorhombic Nb_2O_5 (T-Nb_2O_5, PDF#27-1003). When the annealing temperature reaches 700 °C, the crystal structure of Nb_2O_5 has changed from TT-Nb_2O_5 to T-Nb_2O_5. The crystallite size of the Nb_2O_5 sheets was calculated by the Scherrer equation. The crystallite sizes of the NbO_4, NbO_5, NbO_6 and NbO_7 were 28.6, 35.3, 38.4 and 52.7 nm, respectively. Low calcination temperature causes small crystal size and poor crystallinity, which weakens intensity peaks of NbO_4 and NbO_5 samples [26]. The intensity of the peak for (001) was stronger than the (100) peak demonstrating that the samples oriented-grow at high temperature.

The XPS spectrum of NbO_6 and the components of Nb 3d and O 1s are shown in Figures 2(b-d). Figure 2(c) exhibits that the binding energies at 207.4 and 210.2 eV are consistent with the binding energy for the standard Nb^{5+} in Nb_2O_5 [27]. As shown in Figure 2(d), the peak appearing at 529.6 eV reveals that the valence of O is −2 in NbO_6, and the peak centered at about 533 eV is associated with the surface oxygen [28]. XPS characterization results indicate that the Nb^{4+} in $NbSe_2$ is converted to Nb^{5+} during calcination, corresponding to the formation of Nb_2O_5.

The morphologies and nanostructures of the $NbSe_2$ and Nb_2O_5 sheets are observed by HRSEM. As shown in Figure 3, all the samples show hexagonal sheet structure. The raw material $NbSe_2$ (Figures 3(i), (j)) shows good hexagonal sheet and flat surface morphology. The pores of Nb_2O_5 sheets

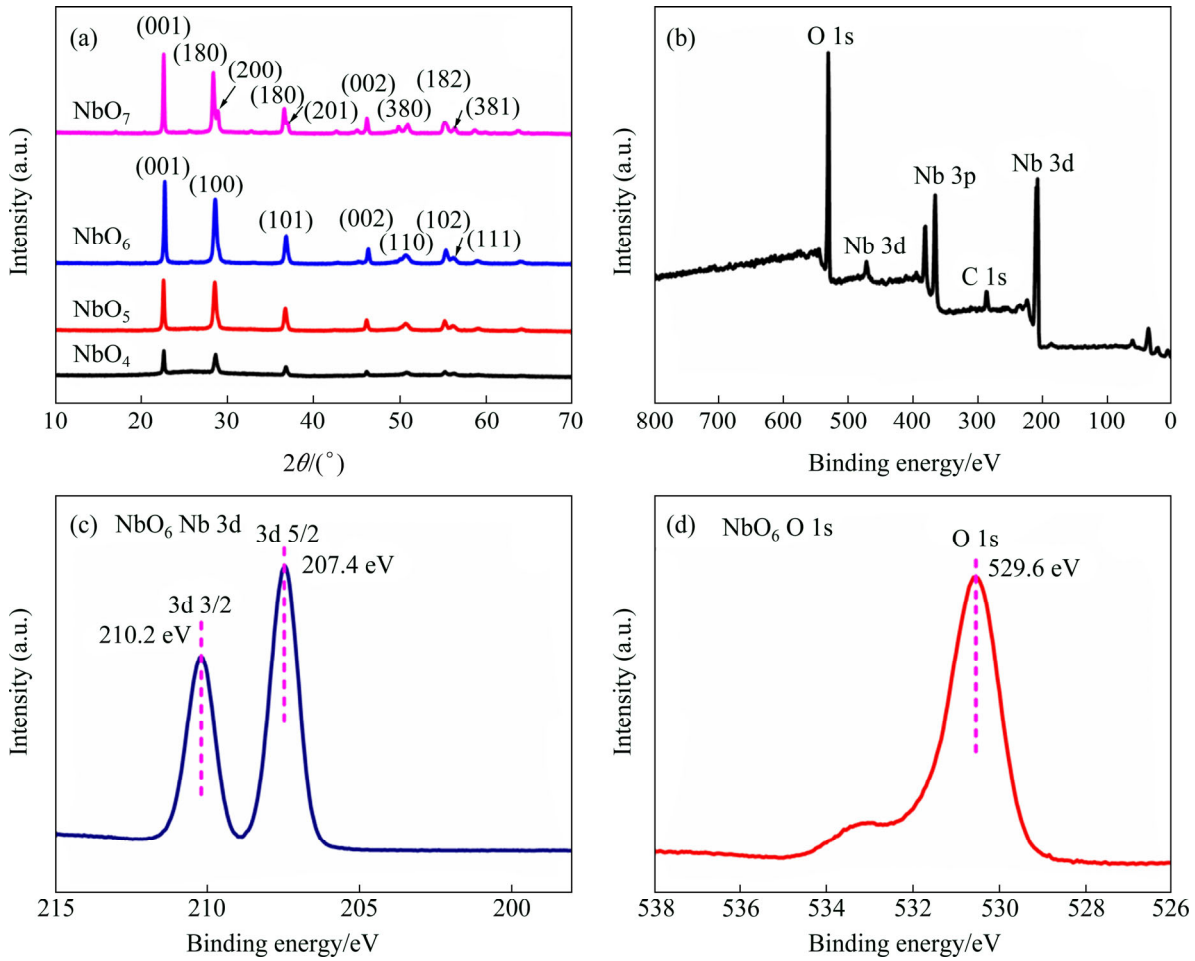

Figure 2 XRD patterns of Nb_2O_5 calcined at different temperatures (a) and XPS spectrum of wide survey of NbO_6 (b), Nb 3d spectrum (c) and O 1s spectrum (d)

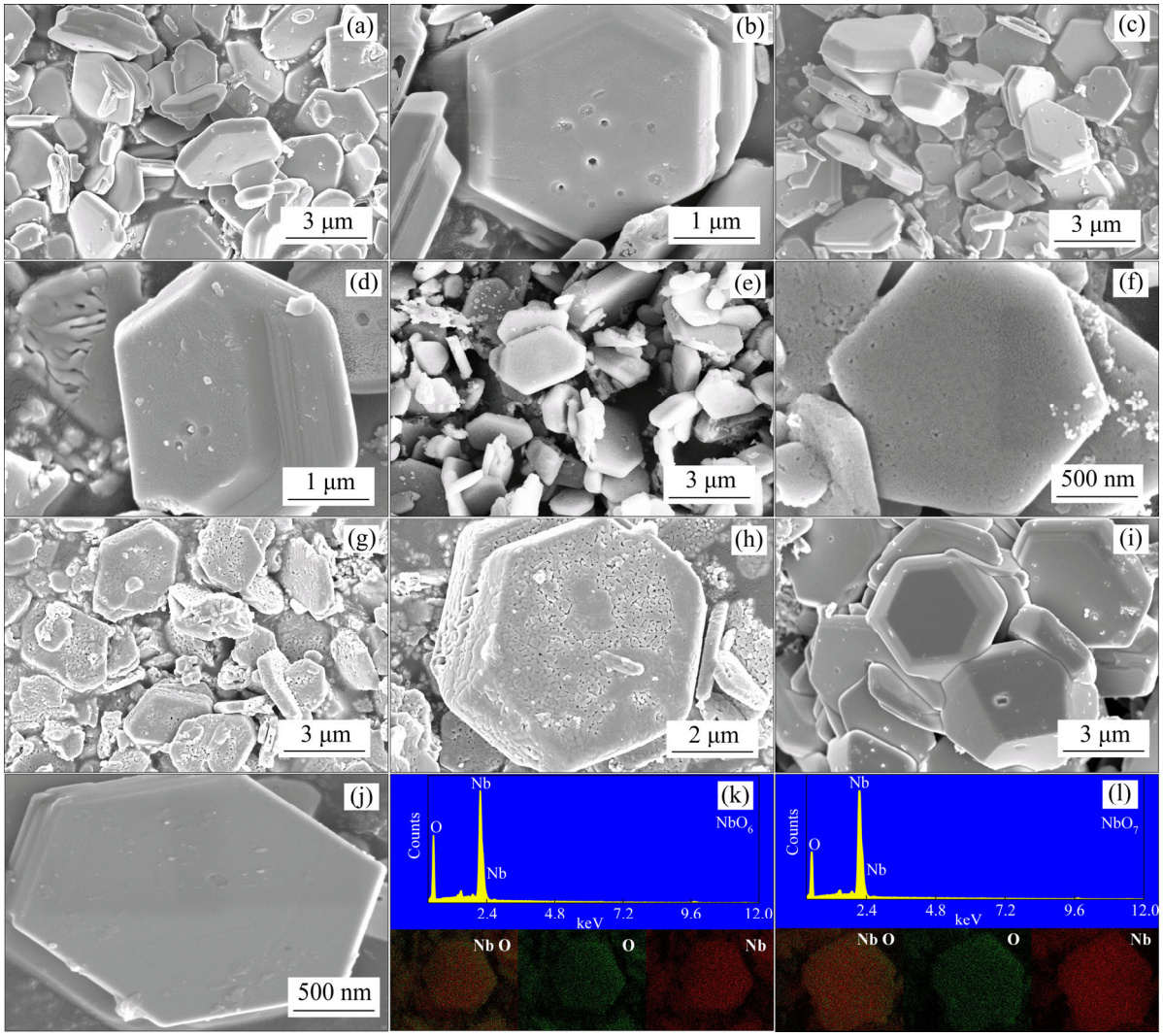

Figure 3 SEM images of NbO_4 (a, b), NbO_5 (c, d), NbO_6 (e, f), NbO_7 (g, h), $NbSe_2$ (i, j) and EDS elemental mapping images of NbO_6 and NbO_7 (k, l)

is due to the volatilization of selenium during calcination in air. The reaction equation can be expressed as:

$$4NbSe_2+5O_2=2Nb_2O_5+8Se \quad (1)$$

As temperature increases, the faster speed of volatilization leads to more pores on the sample surface. When temperature reaches 600 °C, small cracks appear on the sample surface. Figure 3(k) and Figure 3(l) display mapping images of NbO_6 and NbO_7. The single color Nb, O and the mixing color images display homogeneous element distribution in the samples. There is no selenium residue in the samples, suggesting that the as-prepared samples are pure Nb_2O_5. The NbO_6 (Figure 4(a)) and NbO_7 (Figure 4(b)) show regular hexagonal sheet, which are in good agreement with SEM results. Furthermore, the lattice fringes of NbO_6 and NbO_7 can be measured from the HRTEM images, indicating the presence of a well-defined crystal structure. Figures 4(c) and (d) show clear lattice fringes with *d*-spacing of 0.32 nm for NbO_6 and 0.38 nm for NbO_7, which are well matched to the interplanar spacings of (100) plane of TT-Nb_2O_5 (PDF#28-0317) and (001) plane of T-Nb_2O_5 (PDF#27-1003), respectively [29].

Figure 5 displays the N_2-adsorption-desorption isotherms of all samples and the results are listed in Table 1. NbO_4 exhibits the largest specific surface area of 26.043 m^2/g. As the calcination temperature raises, the mean pore diameter of Nb_2O_5 sheets gradually increases, leading to a decrease of mesopores, which in turn leads to the decrease of specific surface area. The mean pore diameter of Nb_2O_5 sheets (Table 1) indicates that mesopores (2−50 nm) are predominantly present in Nb_2O_5

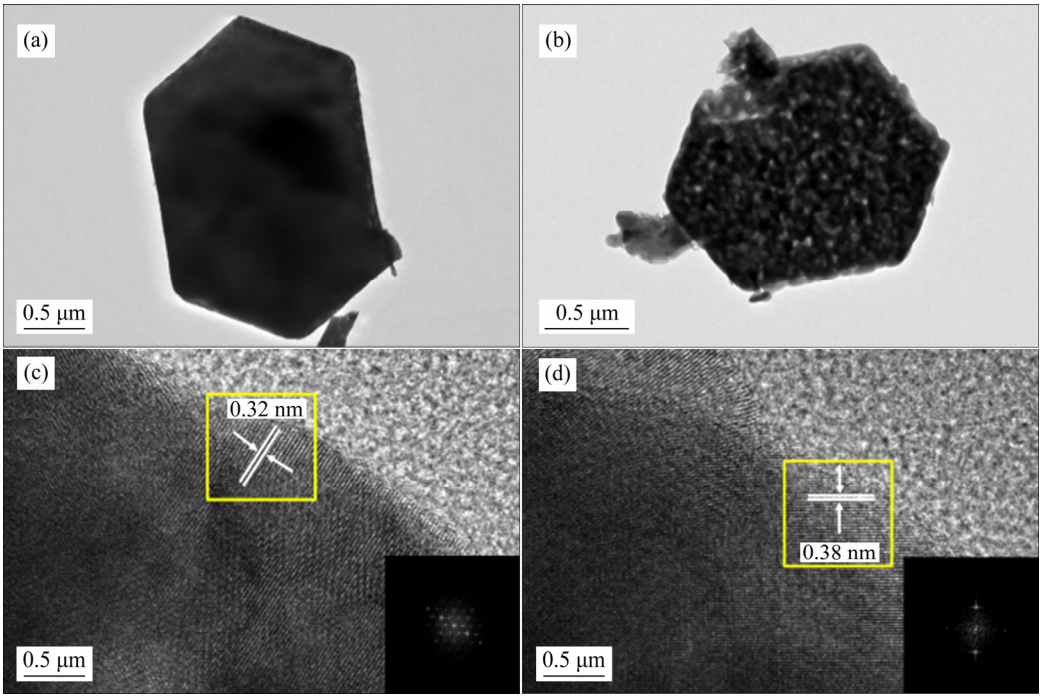

Figure 4 TEM and HRTEM images of NbO_6 (a, c) and NbO_7 (b, d)

Table 1 Specific surface area and average pore diameter

Sample	Specific surface area/($m^2 \cdot g^{-1}$)	Mean pore diameter/nm
NbO_4	26.043	7.9001
NbO_5	20.369	12.626
NbO_6	12.083	21.676
NbO_7	8.788	24.267

sheets. Figure 5(e) indicates the schematic diagram of mesopore mechanism. The electrolyte can penetrate into mesoporous and facilitate the diffusion of lithium ions.

3.2 Electrochemical characterization

Figure 6 shows the initial two cyclic voltammetry (CV) curves of the NbO_4, NbO_5, NbO_6 and NbO_7. All the anodic peaks appear at about 1.8 V, which arise from the variation from Nb^{3+} to Nb^{5+} during Li-ion de-insertion [30]. For NbO_4, NbO_5 and NbO_6, the broad cathodic peak appearing at about 1.75 V can be observed, corresponding to the reduction of Nb^{5+} after lithiation. Compared with the first and second CV curves, the cathodic and anodic peaks almost overlapped, indicating the good reversibility of Li storage properties. In the negative scan process for NbO_7, two reduction peaks are located at around 1.8 and 1.5 V, corresponding to the reaction of Nb^{5+}/Nb^{4+} and Nb^{4+}/Nb^{3+} [31, 32].

The initial charge and discharge profiles at 0.2*C* are plotted in Figure 7(a). The NbO_4 delivers a high discharge capacity of 251 mA·h/g, but a low charge capacity of 126 mA·h/g. With the increase of calcining temperature, the charge capacity of NbO_5, NbO_6 and NbO_7 increases to 134, 178 and 168 mA·h/g, respectively. NbO_6 sample shows the highest charge capacity. Initial coulombic efficiencies of NbO_4, NbO_5, NbO_6 and NbO_7 are 50%, 57%, 68%, 83%, respectively. The low initial coulombic efficiency is highly related to the poor reversibility of the conversion reaction [33]. Figures 7(b) and (c) present the cycling performance of four samples at current density of 0.2*C* and 1*C*, respectively. NbO_6 electrode delivers the highest charge capacity of 178 mA·h/g after 50 cycles at 0.2*C*, with capacity retention rate of 100%. Contrastively, NbO_4, NbO_5 and NbO_7 exhibit charge capacity of 115, 117 and 162 mA·h/g, corresponding to capacity retention ratios of 88%, 91% and 95%, respectively. At current density of 1*C*, the charge capacity of NbO_6 is 158 mA·h/g after 200 cycles, with a high capacity retention rate of 95% (Figure 7(c)). The excellent cycle performance of NbO_6 can be attributed to its high crystallinity (TT-Nb_2O_5). Although the NbO_7 owns another crystal structure (T-Nb_2O_5), it exhibits greater charge capacity (168 mA·h/g) and cycle

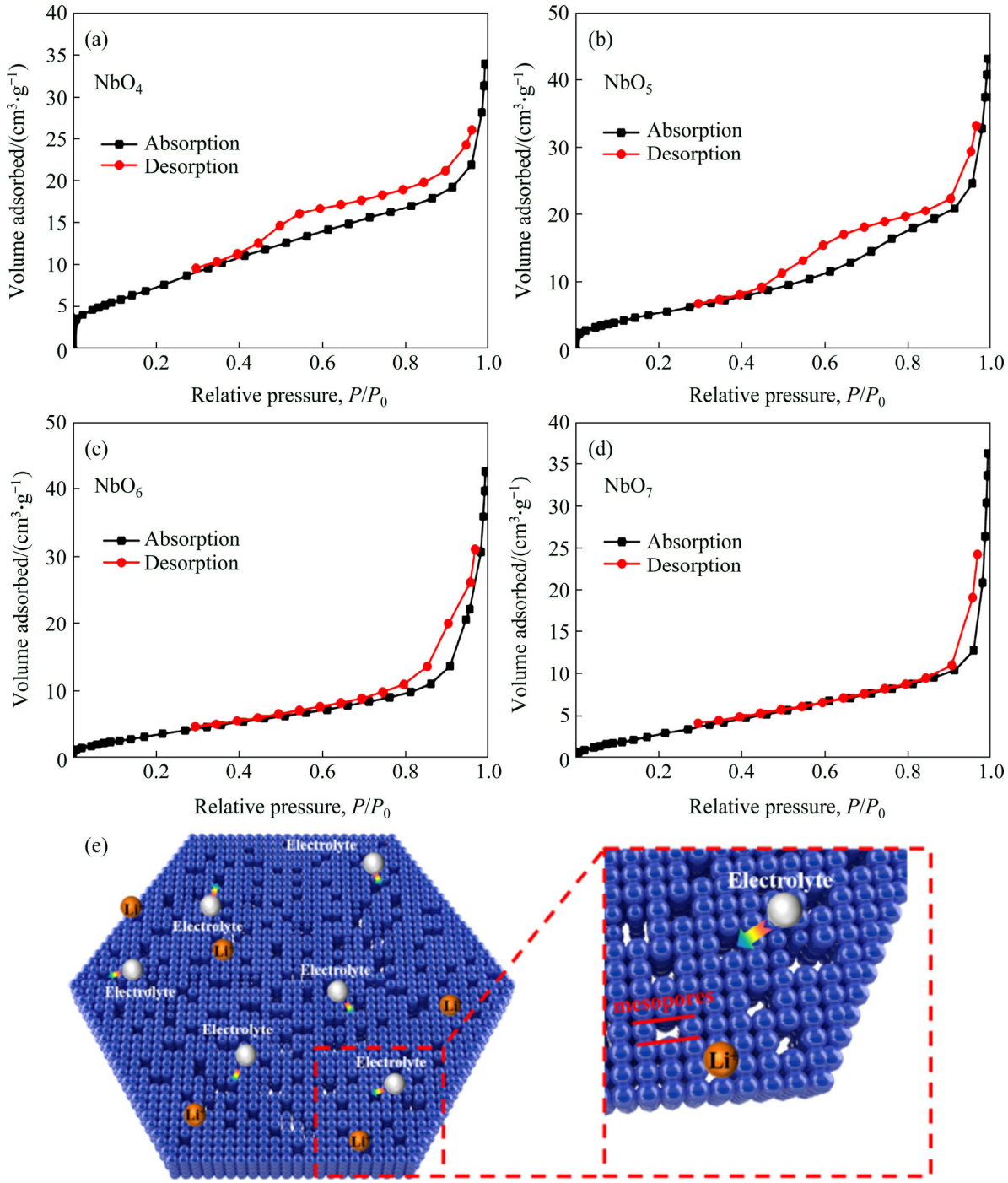

Figure 5 N_2-adsorption-desorption isotherms of NbO_4 (a), NbO_5 (b), NbO_6 (c), NbO_7 (d) and schematic diagram of mesopore mechanism (e)

stability (capacity retention of 92% over 200 cycles at 1*C*) than NbO_4 and NbO_5 samples. Figure 7(d) compares the rate capability of all four electrodes at the rate of 0.2*C* to 20*C*. NbO_6 still exhibited the highest capacities at various rates. When the current density increased to 20*C*, the charge capacity of NbO_6 decreased to 86 mA·h/g. Ultra-stable rate characteristics of the NbO_6 sample in this work were compared with other Nb_2O_5 materials in previously reported (Figure 7(e)). The results suggest that rate performance of NbO_6 in this work was outstanding.

The mechanism of the better performance of TT-Nb_2O_5 (NbO_6) was studied based on pseudocapacitive effect. CV tests were carried out at various scan rates to quantitatively determine the pseudocapacitive effect. As depicted in Figures 8(a) and (b), all the CV curves show similar shapes with

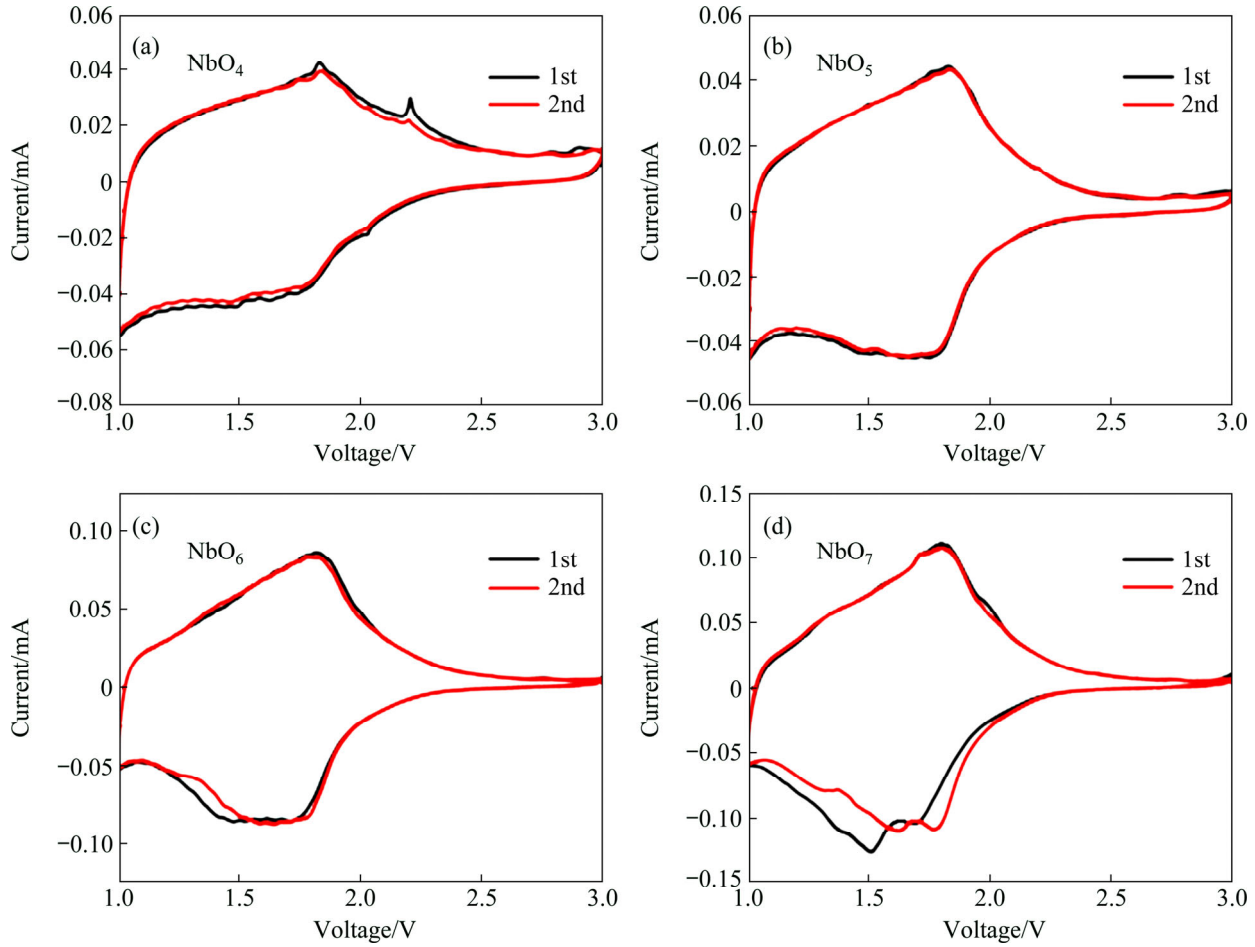

Figure 6 Cyclic voltammograms recorded for NbO_4 (a), NbO_5 (b), NbO_6 (c), NbO_7 (d) at a scan rate of 0.1 mV/s in voltage range of 1.0−3.0 V

almost no peak separations during anodic and cathodic process. Therefore, it can be indicated that the obtained materials present well capacity retention at higher sweep rates. The bump shape of the CV curves exhibited typical pseudocapacitive Li^+ intercalation mechanism [34]. The electrochemical kinetics data can be analyzed by the CV curves following a power law [35]:

$$i=av^b \quad (2)$$

where i is the peak current of each CV curve, v is the sweep rate and a, b are adjustable values. When b is 0.5, it means a diffusion-controlled process ascribed to Li^+ intercalation and transportation. When b is 1, it represents that the current is surface-controlled [36]. In order to determine the b-value, the power law can be transferred as:

$$\lg i=b\lg v+\lg a \quad (3)$$

By plotting lg$i$ vs lg$v$ corresponding to anodic and cathodic peak current from 0.1 to 5 mV/s, the b-value can be obtained from the slope after linear fitting. As seen, the b-values of anodic and cathodic peaks of NbO_6 and NbO_7 are 0.97/1.09 and 0.79/0.90, respectively, showing that the current is almost surface-controlled. In order to determine the respective current contribution from capacitive effect and diffusion-controlled process, equation (2) can be rewritten as [37]:

$$i=k_1v+k_2v^{1/2} \quad (4)$$

where k_1v is capacitive current and $k_2v^{1/2}$ is diffusion current. Both k_1 and k_2 can be determined from the slope and intercept of the linear relationship of $i/v^{1/2}$ and $v^{1/2}$. The CV curves of NbO_6 and NbO_7 at 5 mV/s are shown in Figures 8(c) and (d), in which the capacitive current (k_1v, blue area) is separated from the total current. In addition, the charge storage contributed by capacitive current and diffusion current at other scan rates is calculated as shown in Figures 8(e) and (f). The ratio of capacitive contribution for NbO_6 increases from

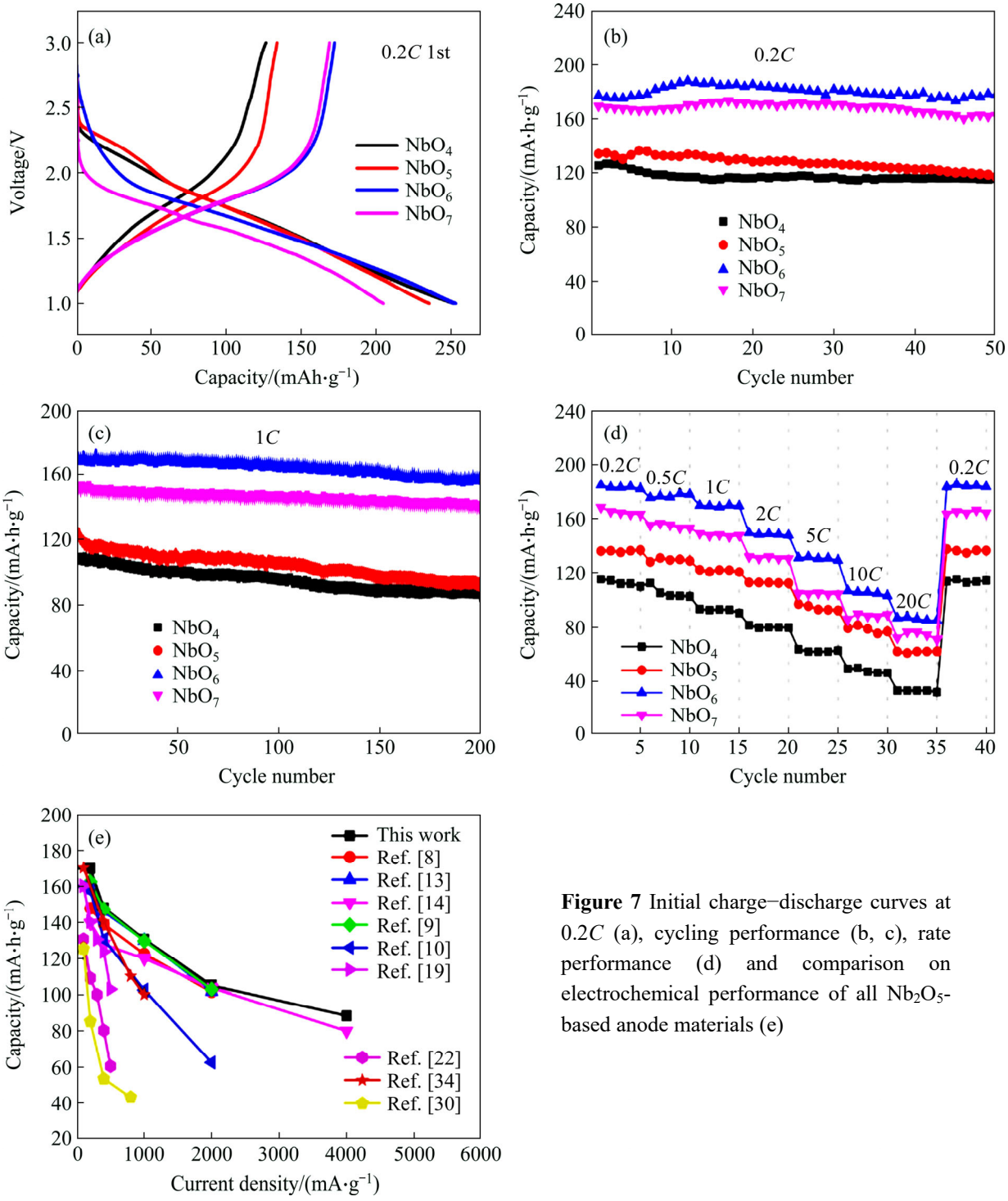

Figure 7 Initial charge−discharge curves at 0.2*C* (a), cycling performance (b, c), rate performance (d) and comparison on electrochemical performance of all Nb_2O_5-based anode materials (e)

54% to 89%, which is higher than that of NbO_7 (from 37% to 80%). The greater *b* value for NbO_6 (0.97) than NbO_7 (0.79) demonstrates the faster surface-controlled kinetics. The higher ratio of capacitive contribution responses for better rate performance.

EIS measurement was conducted to further investigate the electrochemical kinetics of Nb_2O_5 electrodes (Figure 9). The fresh cells were kept at 1.6 V after 2 cycles at 0.2*C*. Nyquist plots of all four samples consist of arcs at high frequency and straight lines at low frequency, which is corresponding to the charge-transfer resistance (R_{ct}) at the electrode/electrolyte interface and the Warburg impedance (Z_w) arising from the Li^+ diffusion in the bulk lattice, respectively [38, 39]. The electrolyte resistance (R_s) can be obtained from the intercept of the semicircle on the *X*-axis. The

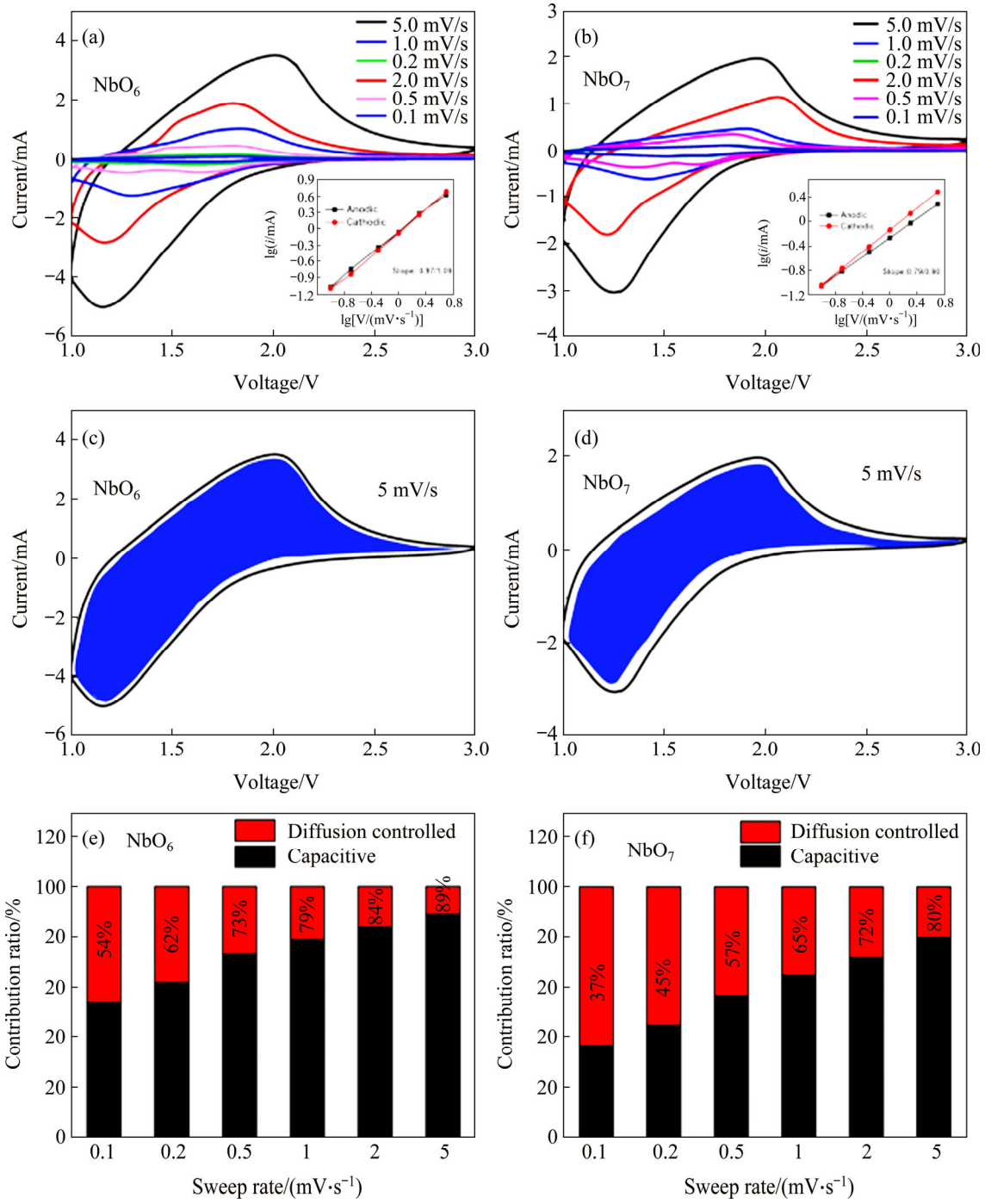

Figure 8 CV curves of NbO_6 (a) and NbO_7 (b) at various sweep rates (v) from 0.1 to 5.0 mV/s (Insets: b values determined by the power law ($\lg i=b\lg v+\lg a$); Separation of the surface capacitive current (k_1v, shadow area) and diffusion currents ($k_2 v^{1/2}$, blank area) at 5.0 mV/s of NbO_6 (c), NbO_7 (d) and pseudocapacitive contribution ratio in the total intercalated charge as a function of sweep rates during CV processes for NbO_6 (e) and NbO_7 (f)

equivalent circuit based on above is inset in Figure 9 [40, 41]. As listed in Table 2, the fitted R_{ct} values are 130.8, 109.9, 65.3 and 65.6 Ω for NbO_4, NbO_5, NbO_6 and NbO_7 electrodes, respectively. The lowest R_{ct} of NbO_6 means the lowest charge transfer resistance and better electrical conductivity, leading to its higher capacity and cycling performance.

Table 2 Impedance parameters of equipment

Temperature/°C	R_s/Ω	R_{ct}/Ω
400	2.31	130.8
500	2.03	109.9
600	1.01	65.3
700	1.25	69.6

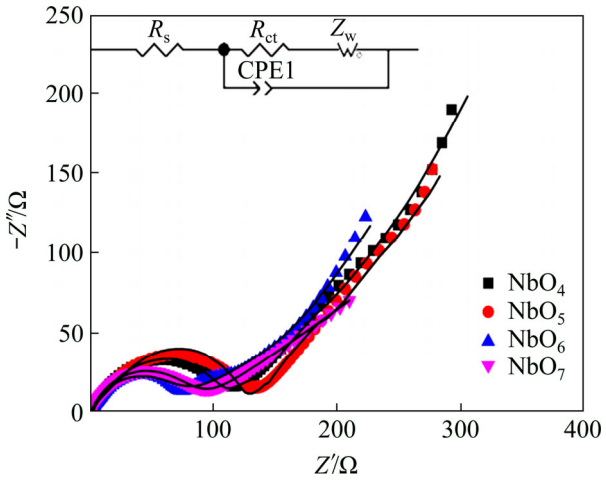

Figure 9 Nyquist plots and equivalent circuit of all four electrodes

4 Conclusions

In summary, a novel hexagonal porous TT-Nb_2O_5 sheet has been successfully synthesized for the first time by facile solid stated reaction for LIBs anode. Reaction temperature has important influence on the structure and electrochemical performance of Nb_2O_5. Nb_2O_5 with high crystallization and small specific surface area was prepared at high temperature. TT-Nb_2O_5 synthesized at 600 °C exhibits the best electrochemical performance. A reversible capacity of 178 mA·h/g can be retained after 50 cycles at 0.2*C*. When cycling at 20*C*, the charge capacity of TT-Nb_2O_5 can still deliver 86 mA·h/g. The largest capacity and lower charge transfer resistance of TT-Nb_2O_5 were due to its favorable crystal structure. High ratio of the intercalation pesudocapacitance makes the TT-Nb_2O_5 electrode have more excellent rate performance than T-Nb_2O_5. The present results emphasize that Nb_2O_5 with high crystallization and large specific surface area is a very promising anode material.

Contributors

LIU Yun-jian provided the concept and edited the draft of manuscript. ZHOU Yu conducted the literature review, and wrote the first draft of the manuscript, and replied to reviewers' comments. LIU Ke, ZHOU Yue and NI Jia-hua provided the measured dataand analyzed the measured data. DOU Ai-chun and SU Ming-ru provided resources and validation. All authors revised the final version.

Conflict of interest

ZHOU Yu, LIU Ke, ZHOU Yue, NI Jia-hua, DOU Ai-chun, SU Ming-ru, LIU Yun-jian declare that they have no conflict of interest.

References

[1] GOODENOUGH J, PARK K. The Li-ion rechargeable battery: A perspective [J]. Journal of the American Chemical Society, 2013, 135: 1167−1176. DOI: 10.1021/ja3091438.

[2] GUAN Pei-yuan, ZHOU Lu, YU Zhen-lu, SUN Yuan-dong, LIU Yun-jian, WU Fei-xiang, JIANG Yi-feng, CHU De-wei. Recent progress of surface coating on cathode materials for high performance lithium-ion batteries [J]. Journal of Energy Chemistry, 2020, 43: 220−235. DOI: 10.1016/j.jechem.2019.08.022.

[3] ZHENG Jun-chao, YANG Zhuo, DAI Alvin, TANG Lin-bo, WEI Han-xin, LI Yun-jiao, HE Zhen-jiang, LU jun. Boosting cell performance of $LiNi_{0.8}Co_{0.15}Al_{0.05}O_2$ via surface structure design [J]. Small, 2019, 15(50): 1904854. DOI: 10.1002/smll.201904854.

[4] QU Xing-yu, YU Zhen-lu, RUAN Ding-shan, DOU Ai-chun, SU Ming-ru, ZHOU Yu, LIU Yun-jian, CHU De-wei, Enhanced electrochemical performance of Ni-rich cathode materials with $Li_{1.3}Al_{0.3}Ti_{1.7}(PO_4)_3$ coating [J]. ACS Sustainable Chemistry & Engineering, 2020, 8(15): 5819−5830. DOI: 10.1021/acssuschemeng.9b05539.

[5] ZHOU Zhi-wei, LUO Zi-yan, HE Zhen-jiang, ZHENG Jun-chao, LI Yun-jiao. A novel hollow porous structure designed for $Na_{0.44}Mn_{2/3}Co_{1/6}Ni_{1/6}O_2$ cathode material of sodium-ion batteries [J]. Journal of Power Sources, 2020, 479: 228788. DOI: 10.1016/j.jpowsour.2020.228788.

[6] WU Ling, HU Yong, ZHANG Xiao-ping, LIU Jie-qun, ZHU Xing, ZHONG Sheng-kui. Synthesis of carbon-coated Na_2MnPO_4F hollow spheres as a potential cathode material for Na-ion batteries [J]. Journal of Power Sources, 2018, 374: 40−47. DOI: 10.1016/j.jpowsour.2017.11.029.

[7] LIU Yi-jian, GUO Hao, ZHANG Bao-hua, WEN Gong-yu, VAJTAI R, WU Ling, AJAYAN P, WANG Liang. Sustainable synthesis of N-doped hollow porous carbon spheres via a spray-drying method for lithium-sulfur storage with ultralong cycle life [J]. Batteries & Supercaps, 2020, DOI: 10.1002/batt.202000143.

[8] WANG Gang, CHEN Yuan-hua, CHEN Chao, KANG Xiong-wu, YANG Cheng-hao, WANG Fei, LIU Yong, XIONG Xun-hui. Self-stabilized and strong adhesive supramolecular polymer protective layer enables ultrahigh rate and large capacity lithium metal anode [J]. Angewandte Chemie Inthernational Edition, 2020, 59: 2055−2060. DOI: 10.1002/anie.201913351.

[9] ZHENG Sheng-quan, DOU Ai-chun, SU Ming-ru, LIU Yun-jian. Influence of Nb doping on electrochemical performance of nanostructured cation disordered $Li_{1+x/100}Ni_{1/2-x/100}Ti_{1/2-x/100}Nb_{x/100}O_2$ composites cathode for Li-ion batteries [J]. Journal of Nanoscience and Nanotechnology, 2020, 20(1): 452−459. DOI:

10.1166/jnn.2020.16884.

[10] FANG Rui, MIAO Chang, MOU Hao-yi, XIAO Wei. Facile synthesis of Si@TiO_2@rGO composite with sandwich-like nanostructure as superior performance anodes for lithium ion batteries [J]. Journal of Alloys and Compounds, 2020, 818: 152884. DOI: 10.1016/j.jallcom.2019.152884.

[11] WU Ling, ZHENG Jie, WANG Liang, XIONG Xun-hui, SHAO Yan-yan, WANG Gang, WANG Jeng-han, ZHONG Sheng-kui, WU Ming-hong. PPy-encapsulated SnS_2 nanosheets stabilized by defects on a TiO_2 support as a durable anode material for lithium-ion batteries [J]. Angew Chem Int Ed Engl, 2018, 58(3): 811−815. DOI: 10.1002/ange.201811784.

[12] YU Zhen-lu, QU Xing-yu, WAN Tao, DOU Ai-chun, ZHOU Yu, PENG Xiao-qi, SU Ming-ru, LIU Yun-jian, CHU De-wei. Synthesis and mechanism of high structural stability of nickel-rich cathode materials by adjusting Li-excess [J]. ACS Appl Mater Interfaces, 2020, 12(36): 40393−40403. DOI: 10.1021/acsami.0c12541.

[13] AUGUSTYN V, COME J, LOWE M, KIM J, TABERNA P, TOLERT S, ABRUNA H, SIMON P, DUNN B. High-rate electrochemical energy storage through Li^+ intercalation pseudocapacitance [J]. Nature Matrials, 2013, 12: 518−522. DOI: 10.1038/nmat3601.

[14] YAN Li-tao, RUI Xian-hong, CHEN Gen, XU Wei-chuan, ZOU Gui-fu, LUO Hong-mei. Recent advances in nanostructured Nb-based oxides for electrochemical energy storage [J]. Nanoscale, 2016, 8: 8443−8465. DOI: 10.1039/C6NR01340F.

[15] KODAMA R, TERADA Y, NAKAI I, KOMABA S, KUMAGAI N. Electrochemical and in situ XAFS-XRD investigation of Nb_2O_5 for rechargeable lithium batteries [J]. Journal of the Electrochemical Society, 2006, 153: 583−588. DOI: 10.1149/1.2163788.

[16] WANG Xu, YAN Chao-yi, YAN Jian, SUMBOJA A, LEE P. Orthorhombic niobium oxide nanowires for next generation hybrid supercapacitor device [J]. Nano Energy, 2015, 11: 765−772. DOI: 10.1016/j.nanoen.2014.11.020.

[17] LIU Xiao-di, LIU Guang-yin, CHEN Hao, MA Jian-min, ZHANG Rui-xue. Facile synthesis of Nb_2O_5 nanobelts assembled from nanorods and their applications in lithium ion batteries [J]. Journal of Physics and Chemistry of Solids, 2017, 111: 8−11. DOI: 10.1016/j.jpcs.2017.07.007.

[18] WANG Hong-xun, ZHANG Bao, ZENG Xian-qing, YAN Li-jing, ZHENG Jun-chao, LING Min, HOU Yang, LU Ying-ying, LIANG Cheng-du. 3D porous carbon nanofibers with CeO_2-decorated as cathode matrix for high performance lithium-sulfur batteries [J]. Journal of Power Sources, 2020, 473: 228588. DOI: 10.1016/j.jpowsour.2020.228588.

[19] CHEONG J, JUNG J, YOUN D, KIM C, YU S, CHO S, YOON K, KIM I. Mesoporous orthorhombic Nb_2O_5 nanofibers as pseudocapacitive electrodes with ultra-stable Li storage characteristics [J]. Journal of Power Sources, 2017, 360: 434−442. DOI: 10.1016/j.jpowsour.2017.06.030.

[20] CHEONG J, YOUN D, KIM C, JUNG J, OGATA A, JIN G. Ag-coated one-dimensional orthorhombic Nb_2O_5 fibers as high performance electrodes for lithium storage [J]. Electrochimica Acta, 2018, 269: 388−396. DOI: 10.1016/j.electacta.2018.03.028.

[21] LIU Guang-yin, JIN Bo, BAO Ke-yan, XIE Hai-quan, GUO Jia-li, JI Xiao-guang, ZHANG Rui-xue, JIANG Qing. Facile synthesis of porous Nb_2O_5 microspheres as anodes for lithium-ion batteries [J]. International Journal of Hydrogen Energy, 2017, 42: 6065−6071. DOI: 10.1016/j.ijhydene.2016.11.126.

[22] LOU Shuai-feng, CHENG Xin-qun, WANG Long, GAO Jin-long, LI Qin, MA Yun-lin, GAO Yun-zhi, ZUO Peng-jian, DU Chun-yu, YIN Ge-ping. High-rate capability of three-dimensionally ordered macroporous T-Nb_2O_5 through Li^+ intercalation pseudocapacitance [J]. Journal of Power Sources, 2017, 361: 80−86. DOI: 10.1016/j.jpowsour.2017.06.023.

[23] LU Shi-jie, WANG Zhi-teng, ZHANG Xia-hui, HE Zhen-jiang, TONG Hui, LI Yun-jiao, ZHENG Jun-chao. In situ-formed hollow cobalt sulfide wrapped by reduced graphene oxide as an anode for high-performance lithium-ion batteries [J]. ACS Appl Mater Interfaces, 2020, 12(2): 2671−2678. DOI: 10.1021/acsami.9b18931.

[24] HUO Yi-feng, QIN Ning, LIAO Cheng-zhu, FENG Hui-fen, GU Ying-ying, CHENG Hua. Hydrothermal synthesis and energy storage performance of ultrafine $Ce_2Sn_2O_7$ nanocubes [J]. Journal of Central South University, 2019, 26(6): 1416−1425. DOI: 10.1007/s11771-019-4097-4.

[25] LIU Yu-bin, LIN Li-wei, ZHANG Wei-feng, WEI Ming-deng. Heterogeneous TiO_2@Nb_2O_5 composite as a high-performance anode for lithium-ion batteries [J]. Scientific Reports, 2017, 7: 7204. DOI: 10.1038/s41598-017-07562-5.

[26] LIU Xiao-di, DUAN Xiao-chuan, PENG Peng, ZHENG Wen-jun. Hydrothermal synthesis of copper selenides with controllable phases and morphologies from an ionic liquid precursor [J]. Nanoscale, 2011, 3: 5090−5095. DOI: 10.1039/C1NR10833F.

[27] CAO Dun-ping, YAO Zhen-guo, LIU Jian-jun, ZHANG Jin-cang, LI Chi-lin. H-Nb_2O_5 wired by tetragonal tungsten bronze related domains as high-rate anode for Li-ion batteries [J]. Energy Storage Materials, 2018, 11: 152−160. DOI: 10.1016/j.ensm.2017.10.005.

[28] VIET A, REDDY M, JOSE R, CHOWDARI B，RAMAKRISHNA S. Nb_2O_5 photoelectrodes for dye-sensitized solar cells: Choice of the polymorph [J]. The Journal of Physical Chemistry C, 2010, 114(49): 21795−21800. DOI: 10.1021/jp106515k.

[29] YUN Si-ning, SI Yi-ming, SHI Jing, ZHANG Tai-hong, HOU Yu-zhi, LIU Hang, MENG Sheng, HAGFELDT A. Electronic structures and catalytic activities of niobium oxides as electrocatalysts in liquid-junction photovoltaic devices [J]. Solar RRL, 2020, 4(3): 1900430. DOI: 10.1002/solr.201900430.

[30] KIM K, KIM M, CHA P, KANG S, KIM J. Structural modification of self-organized nanoporous niobium oxide via hydrogen treatment [J]. Chemistry of Materials, 2016, 28(5): 1453−1461. DOI: 10.1021/acs.chemmater.5b04845.

[31] KONG Ling-ping, ZHANG Chuan-fang, WANG Ji-tong, QIAO Wen-ming, LING Li-cheng, LONG Dong-hui. Free-standing T-Nb_2O_5/graphene composite papers with ultrahigh gravimetric/volumetric capacitance for Li-ion intercalation pseudocapacitor [J]. ACS Nano, 2015, 9(11):

11200−11208. DOI: 10.1021/acsnano.5b04737.

[32] YANG Chao, YU Shu, LIN Chun-fu, LV Fan, WU Shun-qing, YANG Yong, WANG Wei, ZHU Zi-zhong, LI Jian-bao, WANG Ning, GUO Shao-jun. $Cr_{0.5}Nb_{24.5}O_{62}$ nanowires with high electronic conductivity for high-rate and long-life lithium-ion storage [J]. ACS Nano, 2017, 11(4): 4217−4224. DOI: 10.1021/acsnano.7b01163.

[33] HE Han-na, SUN Dan, TANG You-gen, WANG Hai-yan, SHAO Min-hua. Understanding and improving the initial Coulombic efficiency of high-capacity anode materials for practical sodium ion batteries [J]. Energy Storage Materials, 2019, 23: 233−251. DOI: 10.1016/j.ensm.2019.05.008.

[34] LUKATSKAYA M, DUNN B, GOGOTSI Y. Multidimensional materials and device architectures for future hybrid energy storage [J]. Nature Communications, 2016, 7: 12647. DOI: 10.1038/ncomms12647.

[35] RAUDA I, AUGUSTYN V, DUNN B, TOLBERT S. Enhancing pseudocapacitive charge storage in polymer templated mesoporous materials [J]. Accounts of Chemical Research, 2013, 46(5): 1113−1124. DOI: 10.1021/ar300167h.

[36] WANG Ru-tao, LANG Jun-wei, ZHANG Peng, LIN Zong-yuan, YAN Xing-bin. Fast and large lithium storage in 3D porous VN nanowires-graphene composite as a superior anode toward high performance hybrid supercapacitors [J]. Advanced Functional Materials, 2015, 25(15): 2270−2278. DOI: 10.1002/adfm.201404472.

[37] LI Guang-chao, YIN Zhou-lan, GUO Hua-jun, WANG Zhi-xing, YAN Guo-chun, YANG Zhe-wei, LIU Yong, JI Xiao-bo, WANG Jie-xi. Metalorganic quantum dots and their graphene-like derivative porous graphitic carbon for advanced lithium-ion hybrid supercapacitor [J]. Advanced Energy Materials, 2019, 9(2): 1802878. DOI: 10.1002/aenm.201802878.

[38] YANG Shu-qi, WANG Peng-bo, WEI Han-xin, TANG Lin-bo, ZHANG Xia-hui, HE Zhen-jiang, LI Yun-jiao, TONG Hui, ZHENG Jun-chao. $Li_4V_2Mn(PO_4)_4$ stablized $Li[Li_{0.2}Mn_{0.54}Ni_{0.13}Co_{0.13}]O_2$ cathode materials for lithium ion batteries [J]. Nano Energy, 2019, 63: 103889. DOI: 10.1016/j.nanoen.2019.103889.

[39] TAN Yu-ming, CHEN Xian-hong, ZHU Yi-rong, CHEN Li-juan. Synthesis of spherical tremella-like Sb_2O_3 structures derived from metal-organic framworks and its lithium storage properties [J]. Journal of Central South University, 2019, 26: 1469−1480. DOI: 10.1007/s11771-019-4103-x.

[40] ZHOU Xiao-zhong, LU He-jie, TANG Xing-chang, ZENG Ya-ping, YU Xin. Facile synthesis of Sb@Sb_2O_3/reduced graphene oxide composite with superior Lithium-storage performance [J]. Journal of Central South University, 2019, 26(6): 1493−1502. DOI: 10.1007/s11771-019-4105-8.

[41] FANG Rui, XIAO Wei, MIAO Chang, MEI Ping, YAN Xue-ming, ZHANG Yan, JIANG Yu. Improved lithium storage performance of pomegranate-like Si@NC/rGO composite anodes by facile in-situ nitrogen doped carbon coating and freeze drying processes [J]. Journal of Alloys and Compounds, 2020, 834: 155230. DOI: 10.1016/j.jallcom.2020.155230.

(Edited by HE Yun-bin)

中文导读

六方多孔 TT-Nb_2O_5 微米片的固相制备与储锂性能

摘要：本文通过固相反应首次合成了一种六方多孔 Nb_2O_5 材料。通过优化热处理温度调节 Nb_2O_5 材料的结构和电化学性能。XRD 结果表明，在不同温度下可以合成伪六方晶系与正交晶系 Nb_2O_5；SEM 结果表明，所合成的 Nb_2O_5 材料具有正六边形貌与多孔结构。将该材料用作锂离子电池负极材料时，在 600 ℃制备的伪六方结构 Nb_2O_5(TT-Nb_2O_5)表现出最优的电化学性能。0.2*C* 电流密度下，其可逆比容量为 178 mA·h/g；当电流密度提高到 20*C* 时，可逆比容量仍有 86 mA·h/g。优异的电化学性能得益于 Nb_2O_5 的赝电容式锂离子嵌入机制，通过晶体结构与比表面积调控显著提高 Nb_2O_5 的综合电化学性能。

关键词：锂离子电池；五氧化二铌；六方多孔；电化学性能